Rock Mech Rock Eng (2016) 49:3597–3614
DOI 10.1007/s00603-016-1001-5

ORIGINAL PAPER

Numerical Investigation into the Influence of Bedding Plane on Hydraulic Fracture Network Propagation in Shale Formations

Zou Yushi[1] · Ma Xinfang[1] · Zhang Shicheng[1] · Zhou Tong[1] · Li Han[2]

Received: 22 August 2015 / Accepted: 2 May 2016 / Published online: 17 May 2016
© Springer-Verlag Wien 2016

Abstract Shale formations are often characterized by low matrix permeability and contain numerous bedding planes (BPs) and natural fractures (NFs). Massive hydraulic fracturing is an important technology for the economic development of shale formations in which a large-scale hydraulic fracture network (HFN) is generated for hydrocarbon flow. In this study, HFN propagation is numerically investigated in a horizontally layered and naturally fractured shale formation by using a newly developed complex fracturing model based on the 3D discrete element method. In this model, a succession of continuous horizontal BP interfaces and vertical NFs is explicitly represented and a shale matrix block is considered impermeable, transversely isotropic, and linearly elastic. A series of simulations is performed to illustrate the influence of anisotropy, associated with the presence of BPs, on the HFN propagation geometry in shale formations. Modeling results reveal that the presence of BP interfaces increases the injection pressure during fracturing. HF deflection into a BP interface tends to occur under high strength and elastic anisotropy as well as in low vertical stress anisotropy conditions, which generate a T-shaped or horizontal fracture. Opened BP interfaces may limit the growth of the fracture upward and downward, resulting in a very low stimulated thickness. However, the opened BP interfaces favor fracture complexity because of the improved connection between HFs and NFs horizontally under moderate vertical stress anisotropy. This study may help predict the HF growth geometry and optimize the fracturing treatment designs in shale formations with complex depositional heterogeneity.

Keywords Shale · Bedding plane · Natural fracture · Anisotropy · Hydraulic fracture network

List of symbols

p	Fluid pressure within the fracture
p_{int}	Initial fluid pressure within the fracture
μ	Fluid dynamic viscosity
Q_{t}	Total injection rate
q	Local flow rate within the fracture
$F_{\mathrm{n}},\ F_{\mathrm{s}}$	Normal and shear forces on a contact
$k_{\mathrm{n}},\ k_{\mathrm{s}}$	Normal and shear contact stiffness
$F_{\mathrm{n}}^{\max},\ F_{\mathrm{s}}^{\max}$	Tensile and shear bond strengths of a contact
$F_{\mathrm{fric}}^{\mathrm{s}}$	Friction force of a contact
$u_{\mathrm{n}},\ u_{\mathrm{s}}$	Normal and shear displacements
$\Delta u_{\mathrm{n}},\ \Delta u_{\mathrm{s}}$	Normal and shear displacement increments
w	Fracture aperture
w_{res}	Fracture residual aperture
σ_{ij}	Cauchy stress tensor
b_i	Body force per unit volume
$u_{i,t},\ u_{i,tt}$	Velocity and acceleration
ρ	Rock density
α	Damping coefficient
D	Elasticity tensor
ε	Strain tensor
A	Contact area
G_{v}	Shear modulus parallel to bedding plane

✉ Zou Yushi
zouyushi@126.com

[1] China University of Petroleum, Beijing, China

[2] Texas A&M University, College Station, TX, USA

E_h, E_v	Young's moduli parallel and perpendicular to bedding plane
ν_h, ν_v	Poisson's ratios parallel and perpendicular to bedding plane
T_{0h}, T_{0v}	Tensile strengths parallel and perpendicular to bedding plane
S_{0h}, S_{0v}	Cohesions parallel and perpendicular to bedding plane
φ_{0h}, φ_{0v}	Frictional angles parallel and perpendicular to bedding plane
k_h, k_v	Permeability parallel and perpendicular to bedding plane
k_{nf}	Permeability of natural fracture
T_{nf}	Tensile strength of natural fracture
S_{nf}	Cohesion of natural fracture
φ_{nf}	Frictional angle of natural fracture
σ_{hmax}, σ_{hmin} and σ_v	Maximum, minimum horizontal and vertical in situ stresses
$\Delta\sigma_h$, $\Delta\sigma_v$	Horizontal and vertical stress anisotropies
θ	Intersection angle between hydraulic fracture and natural fracture

1 Introduction

Multistage hydraulic fracturing of a horizontal well is required for the development of shale formations in which a large-scale hydraulic fracture network (HFN) is generated to transport hydrocarbons to a wellbore. The stimulated reservoir volume has been interpreted by microseismic mapping (Fisher et al. 2002; Warpinski et al. 2005). To simulate the hydraulic fracturing process in naturally fractured formations while considering the effect of natural fractures (NFs) and multiple fracture interactions, models of varying complexity have been developed. Xu et al. (2010) and Meyer and Bazan (2011) proposed a wire-mesh model and a discrete fracture network model, respectively. In both these pseudo-3D models, the HFN geometry is represented by an elliptical region with two sets of parallel and uniformly spaced vertical fractures along the directions of horizontal principal stress. Weng et al. (2011) presented a pseudo-3D-based complex network model known as the unconventional fracture model. Similar to the wire-mesh model and discrete fracture network model, the unconventional fracture model considers some important features that are expected to be involved in a fracturing treatment simulation, such as proppant transport, non-Newtonian fluid behavior, and wellbore and perforation parameters. More importantly, it can simulate the creation of complex HFNs by considering both the criteria of HF–NF interaction and the interference among adjacent fractures by calculating the "stress shadow."

Several other rock-mechanics-based numerical methods have been used to study HFN generation. Olson (2008) and Olson and Dahi-Taleghani (2009) described a pseudo-3D boundary element method (BEM)-based HFN model where multiple fractures growth satisfies the subcritical power law, and both tensile and shear failures are considered while assuming a constant and uniform hydraulic pressure within the fractures. Dahi-Taleghani and Olson (2009, 2014) presented a 2D plane-strain extended finite element method (XFEM) model which can simulate the creation of asymmetric fracture wings and the diversion of the fracture path along NFs. The above-mentioned BEM and XFEM, which are classified as continuum-based methods, can efficiently treat the fractures of arbitrary pathways without re-meshing. Many significant studies have also been conducted by utilizing the commercially available codes PFC2D, UDEC, and 3DEC (Nagel et al. 2013; Nasehi and Mortazavi 2013; Hamidi and Mortazavi 2014). These are based on a discontinuum method, commonly known as the discrete element method (DEM). In this method, the formation comprises numerous mutually bonded particles (in PFC2D) or deformable blocks (in UDEC and 3DEC), and several sets of joints between all neighboring particles or blocks form a flow network to generate HFs (Itasca Consulting Group Inc., 2014). Compared with continuum methods, the advantage of this method is that the dense preexisting discontinuities or contacts between the blocks as well as their mechanical behavior during HF development in a fractured rock mass can be appropriately modeled. DEM was comprehensively introduced in the latest review by Lisjak and Grasselli (2014). Weng (2015) presented an overview of the hydraulic fracturing models developed and applied to simulate complex fractures in naturally fractured formations.

All models mentioned so far considered the formations as isotropic, and few studies have focused on the effects of formation anisotropy (Zhao et al. 2014). Shale formations are multilayered and typically exhibit anisotropic properties, which result from the existence of bedding planes (BPs) or layer interfaces (Gale et al. 2007; Waters et al. 2011; Mokhtari et al. 2014). Figure 1 shows that numerous NFs and BPs (or layer interfaces) exist in the Longmaxi–Wufeng shale formations in the Sichuan Basin, China. The effects of shale BPs on the complex HFN growth have been directly observed through laboratory fracturing tests (Suarez-Rivera et al. 2013; Guo et al. 2014; Zou et al. 2016). Layer interfaces influence the HF growth in the vertical direction, which was documented through the mine-back experiments or/and fracture mapping (Fisher and Warpinski 2012; Rutledge et al. 2014). Furthermore, the height-growth-limiting mechanism or BP failure

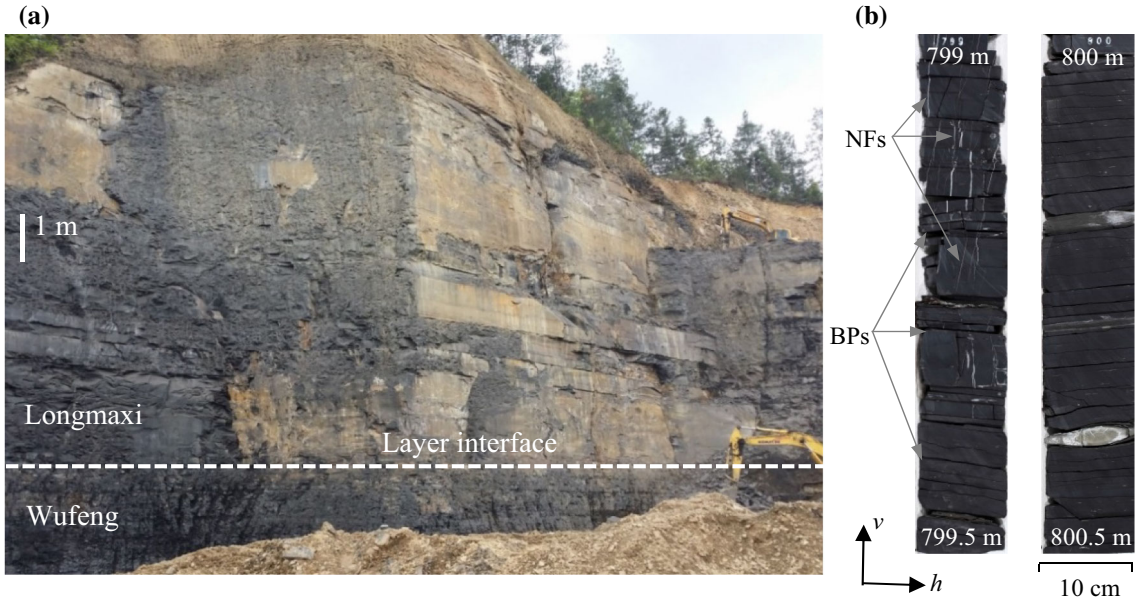

Fig. 1 **a** A shale outcrop exposed area and **b** the core section of the Longmaxi–Wufeng formations in the Sichuan Basin, China. The *horizontal* BPs and *vertical* NFs are visible. The scripts or subscripts *h* and *v* in this study represent the directions parallel and perpendicular to the BP, respectively

mechanism induced by HF has been extensively researched (Hanson et al. 1981; Cooke and Underwood 2001; Zhang et al. 2007; Zhang and Jeffrey 2012; Fisher and Warpinski 2012). A HF encountering a BP may result in four cases: penetration, diversion, offset, and termination (Fig. 2) (Thiercelin et al. 1987). In the first case (Fig. 2a), a HF penetrates through the BP without changing the growth path. In the second case (Fig. 2b), a vertical HF is deflected into the BP and is divided into two branches. A part of or the entire HF may grow along the horizontal BP such that the vertical HF eventually terminates at the BP, forming a T-shaped fracture. Under some conditions, a HF may also re-initiate and leave a step-over at the BP (Fig. 2c). In an extreme case (Fig. 2d), a HF may terminate at the BP. Vertical fracture growth, which is similar to the first case, is implicitly assumed to occur in most existing HF design models. As HFs generally propagate along the path with the least resistance, the assumption can be reasonable in the deep formations, wherein the vertical principal stress is significantly larger than the horizontal minimum principal stress. Fractures mapped in shale formations in North America indicate that the tallest fractures occur in the deepest wells in a specific formation, whereas the shallowest wells in a certain formation generally have the least measured fracture height (Fisher and Warpinski 2012). The constrained height growth in the shallow formations is most likely because of the creation of horizontal fractures. Therefore, the BP effect must be incorporated in complex

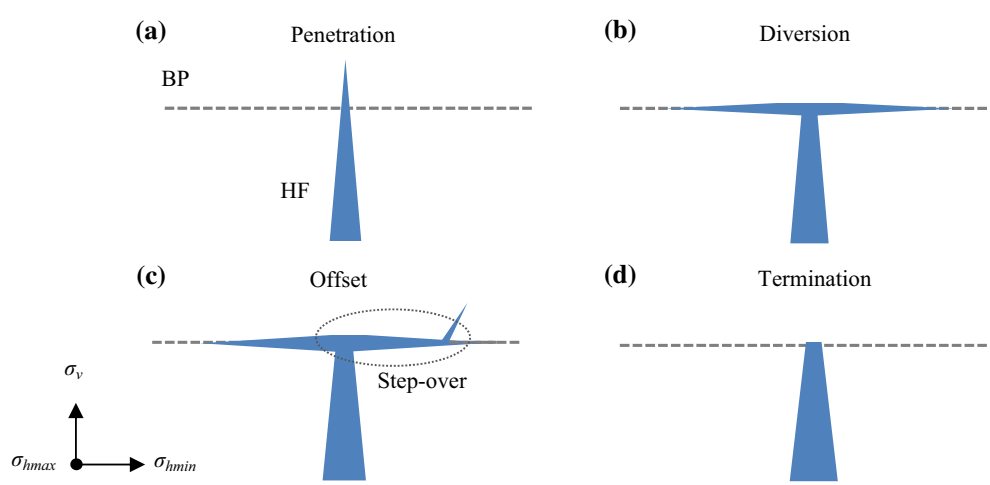

Fig. 2 Four types of HF intersections with a BP interface (Thiercelin et al. 1987)

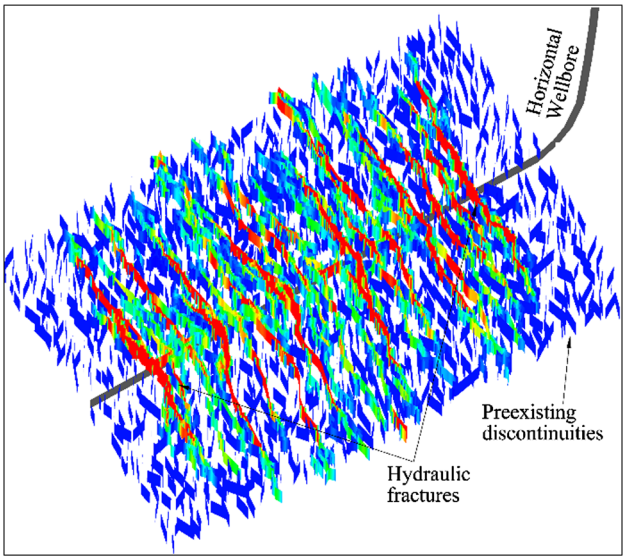

Fig. 3 Shale formation highly fractured by the preexisting discontinuities (e.g., NFs or/and BPs), and multiple hydraulic fractures created during horizontal well fracturing. This is a numerical simulation result where the scattered *blue rectangles* represent the preexisting discontinuities and the other *colors* represent the HFs, which are the same in all the following figures (Color figure online)

fracture models to ensure the accurate prediction of HF growth geometry in shale formations.

During horizontal well fracturing in a shale formation, multiple HFs connect dense preexisting discontinuities such as BPs and NFs, thereby making the shale rock mass highly fractured. This type of shale rock mass can be reasonably referred to as a discontinuous medium, which can be modeled well by the DEM as discussed above (Fig. 3). Hence, this study proposes a HFN propagation model using DEM to examine the resulting HF geometry under different geological conditions in a layered and naturally fractured shale formation. This model is validated against analytical models and published laboratory fracturing test results. The simulation program was coded in C++, and the resulting images were processed using the commercial software TECPLOT.

2 Model Description

Similar to the conventional DEM (Itasca Consulting Group Inc., 2014), the shale rock mass in the current model is divided into several block elements that are bonded by virtual springs (Fig. 4a, b), which transfer interaction forces among blocks. The motion of each block is determined by the magnitude of the resultant unbalanced force that acts on it. The joint elements inserted between all contacting blocks build a continuous flow network (called DFN) for generating HFs. The size, shape, and orientation of this DFN depend on the predefined planes of the BPs and NFs (refer to Sect. 3.1). The fluid pressure distribution inside the fractures is calculated by the finite element method (FEM). The fluid pressure is then exerted on the surrounding blocks (refer to Fig. 4c), resulting in deformations and changes in the stress states at the block contacts. If the stress level at the interface between two blocks exceeds a threshold value either in tension (maximum tensile stress criterion) or in shear (Coulomb criterion), a HF is generated, as shown in Fig. 4d (see Sect. 2.3). The specific numerical method employed in this study is as follows.

2.1 Fluid Flow within the Fractures

The flow of an incompressible and Newtonian fluid within any given fracture with two parallel surfaces is governed by lubrication equations (Batchelor 1967), which are the local mass conservation equation (Eq. 1) and Poiseuille's law (Eq. 2).

$$\frac{\partial w}{\partial t} + \frac{\partial q}{\partial s} = 0, \tag{1}$$

$$q = -\frac{w^3}{12\mu}\frac{\partial p}{\partial s}, \tag{2}$$

where w and p are the fracture aperture and fluid pressure, respectively, at position $s = s\ (x, y, z)$ and time t; q is the local flow rate inside the HFN; and μ is the fluid dynamic viscosity. Given that the shale matrix block is considered impermeable because of its ultra-low permeability, the fluid loss into the matrix is neglected. Therefore, the global mass conservation in the entire HFN is expressed as follows:

$$\int_{\Omega_f} w\ \mathrm{d}s = tQ_t, \tag{3}$$

where Q_t is the total injection rate. Given a single fracturing interval that includes N perforation clusters and a single HF initiated from each perforation cluster, the sum of the flow rates into all fractures should be equal to the total injection rate, i.e., $Q_t = \sum_{i=1}^{N} Q_i$ (Fig. 5). The diversion of the fluid into each fracture depends on the fracture aperture and fluid pressure within the fracture (refer to Eq. 2). Any fracture branch is assumed to be completely filled with fluid, and no flow occurs at the fracture tip. The initial pressure inside the DFN is p_{int}.

2.2 Rock Deformation Equation

In this study, each block of the rock mass is considered to have limited deformability and to be no-rotational (small

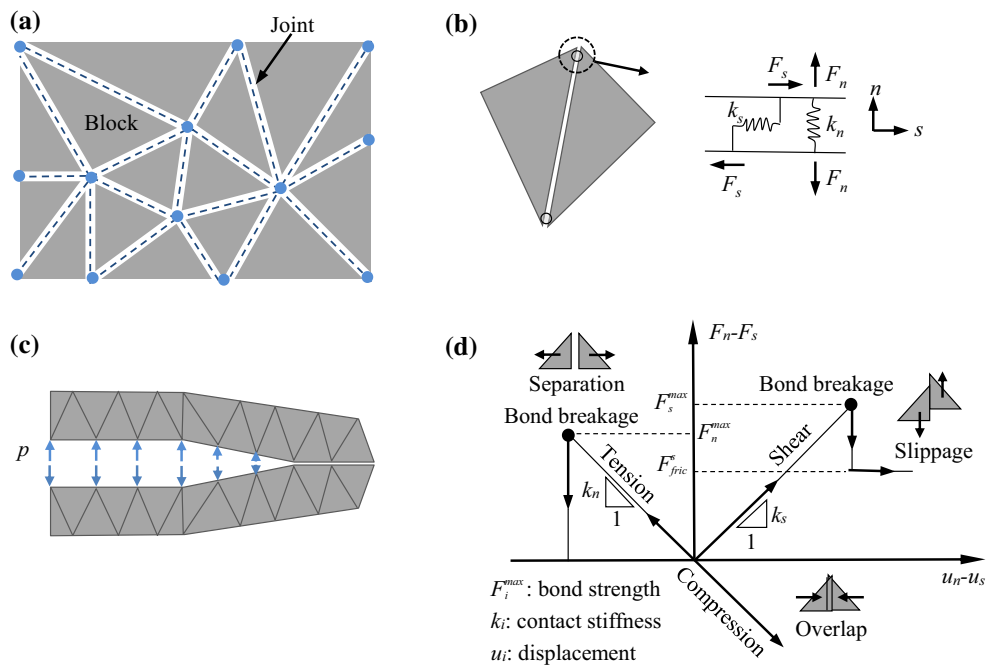

Fig. 4 Modeling HF propagation based on DEM: **a** schematic representation of the discrete block elements (*gray blocks*) and joint elements (*blue dotted lines*); **b** neighboring blocks are bonded together at their contact points with normal and shear springs; **c** fluid pressure (p) within the HF exerted on the boundaries of the block elements; **d** constitutive behavior in tension and shear modes ($i = n$, s). **b**, **d** Are re-drawn according to the study of Kazerani and Zhao (2010) (Color figure online)

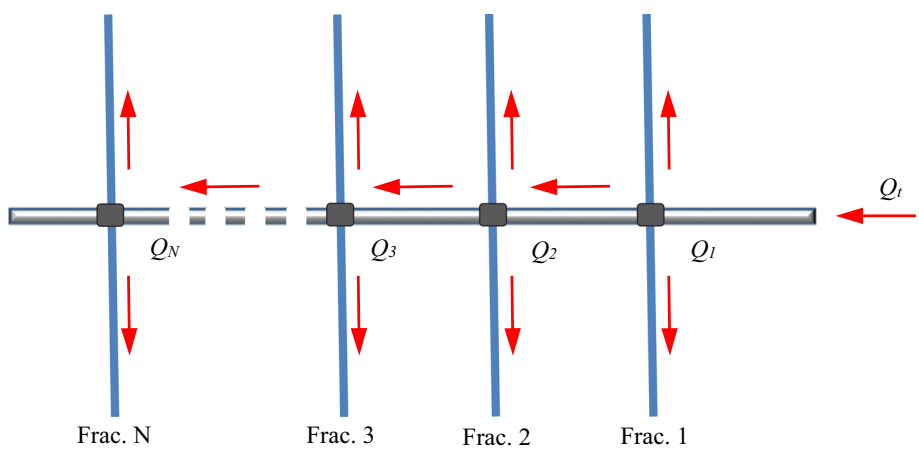

Fig. 5 Illustration of fluid flow distribution. *Red arrows* indicate the directions of the fluid flow during fracturing (Color figure online)

displacement without rotation), and its motion follows Newton's second law. The dynamic stress equilibrium equation for the blocks is as follows (Jaeger et al. 2007):

$$\sigma_{ij,j} + b_i - \rho u_{i,tt} - \alpha u_{i,t} = 0, \tag{4}$$

where σ_{ij} is the Cauchy stress tensor; b_i is the body force per unit volume; $u_{i,t}$ and $u_{i,tt}$ are the velocity and acceleration, respectively; ρ is the rock density; and α is the damping coefficient. The stress induced by the fluid pressure inside the HF can be expressed as

$$\sigma_{ij} \times n_j = p_j, \tag{5}$$

where n_j is the vector normal to the HF surfaces. The stress–strain relationship satisfies the linear elastic constitutive law (Jaeger et al. 2007) such that

$$\sigma_{ij} = D_{ij\mathrm{st}}\varepsilon_{\mathrm{st}}, \tag{6}$$

where $D_{ij\mathrm{st}}$ is the component of the elasticity tensor and $\varepsilon_{\mathrm{st}}$ is the component of the strain tensor. Only two elastic constants are required to describe the full mechanical behavior of an isotropic elastic rock: Young's modulus E and Poisson's ratio ν. However, many shale formations can be characterized as transversely isotropic because of their

layered structure. The implication is that the elastic properties are equal in all directions on a BP (isotropic plane) but different in the direction perpendicular to the BP. In a shale formation with horizontal layers that are oriented perpendicular to the direction of σ_v, the elasticity tensor D is expressed as follows (Itasca Consulting Group Inc., 2014):

$$D = \begin{bmatrix} 1/E_h & -\nu_h/E_h & -\nu_v/E_v & 0 & 0 & 0 \\ -\nu_h/E_h & 1/E_h & -\nu_v/E_v & 0 & 0 & 0 \\ -\nu_v/E_v & -\nu_v/E_v & 1/E_v & 0 & 0 & 0 \\ 0 & 0 & 0 & 2(1+\nu_h)/E_h & 0 & 0 \\ 0 & 0 & 0 & 0 & 1/G_v & 0 \\ 0 & 0 & 0 & 0 & 0 & 1/G_v \end{bmatrix}^{-1}, \tag{7}$$

where five independent elastic constants, including Young's moduli E_h, E_v, Poisson's ratios ν_h, ν_v, and shear modulus G_v, are required to describe linear elastic properties for a transversely isotropic rock. Lekhnitskii (1981) suggested that G_v can be determined through Eq. (8) based on laboratory testing:

$$G_v = \frac{E_v E_h}{E_h(1+2\nu_v)+E_v}. \tag{8}$$

2.3 Interaction of Contacting Blocks and HF Propagation

The mechanical interaction between two contacting blocks is determined by the contact constitutive law (Kazerani and Zhao 2010; Itasca Consulting Group Inc., 2014), as shown in Fig. 4d. Neighboring blocks are initially bonded together at their contact points with the normal and shear springs, which break when the failure criteria (maximum tensile stress criterion and/or Coulomb criterion) are satisfied. The force–displacement (F_n, u_n) and (F_s, u_s) at a contact point in the normal and shear directions, respectively, are governed by the normal contact stiffness k_n, shear contact stiffness k_s, tensile strength T_0, cohesion S_0, and friction angle φ. According to the beam theory, k_n and k_s are related to the Young's modulus E and shear modulus G by $k_n = EA/L$ and $k_s = GA/L$, respectively, where A is the contact area and L is the characteristic length of a contact plane, given by $L = \sqrt{A}$ (refer to Fig. 4b). The maximum possible magnitudes of normal force F_n^{max} and shear force F_s^{max} that the spring can endure at a contact point are calculated as follows:

$$F_n^{max} = AT_0, \tag{9}$$

$$F_s^{max} = AS_0 + \tan\varphi F_n. \tag{10}$$

The updated values of normal and shear forces F_n and F_s at each contact point are calculated after each time step. If $-F_n < F_n^{max}$ (the tensile force is negative) and $|F_s| < F_s^{max}$, no breakage occurs at the contact point, and the normal force F_n and shear force F_s are updated as follows:

$$F_n := F_n - k_n \Delta u_n, \tag{11}$$

$$F_s := F_s - k_s \Delta u_s. \tag{12}$$

If $-F_n \geq F_n^{max}$, the tensile failure occurs at the contact point. The normal force F_n and shear force F_s are then updated as follows:

$$F_n = 0, \tag{13}$$

$$F_s = 0. \tag{14}$$

If $|F_s| \geq F_s^{max}$, the shear failure occurs at the contact point. The normal force F_n and shear force F_s are then updated as follows:

$$F_n := F_n - k_n \Delta u_n, \tag{15}$$

$$F_s = F_{fric}^{s} = \tan\varphi F_n. \tag{16}$$

2.4 Iterative Coupling

The coupling of the fracturing fluid flow inside the DFN and the rock deformation is solved by using an iterative algorithm. By applying the Galerkin FEM, which is one of the weighted residual methods wherein the trial function sequence of the approximate solution is treated as the weight function (Yew 1997), the fluid flow equation was discretized. However, the discrete version of the flow equation is nonlinear because of the direct relation between p and w. The Picard iterative solution method was used to solve this nonlinear equation (Adachi et al. 2007). For each time step, given the trial solution (w_m, p_m), a fixed point strategy based on this approach involves solving the fluid flow equation for p_{m+1}, which is then used in the rock deformation equation to calculate w_{m+1}. If the convergence criterion is not satisfied, the solutions are modified at each internal iteration step as follows:

$$p_{m+1} = (1-\beta)p_m + \beta p_{m+1}, \tag{17}$$

$$w_{m+1} = (1-\beta)w_m + \beta w_{m+1}. \tag{18}$$

This process converges for $0 < \beta < 0.5$ (Adachi et al. 2007). According to the parallel plate model, the relationship between the initial aperture w_0 and permeability k of the fracture can be given as (Zimmerman and Bodvarsson 1996):

$$w_0 = \sqrt{12k}. \tag{19}$$

The matrix permeability in directions parallel and perpendicular to the BP (k_h and k_v) and NF permeability (k_{nf}) must be different; thus, their initial apertures are also different. Moreover, under the compressional stress, two

neighboring blocks may interact by embedding and overlapping each other, which will lead to the closure of the fracture existing between them (Fig. 4d). Hence, a residual fracture aperture w_{res}, which is equal to the initial fracture aperture w_0 in the present study, should be defined to guarantee the convergence and stability in solving the flow equation. Figure 4d shows that the fracture aperture w is equal to the normal relative displacement u_n between the two contacting blocks. Equation (4) is solved by the dynamic relaxation technique, which is an explicit time-domain integration scheme. For details on this solution method, please refer to the Itasca Consulting Group Inc., (2014).

3 Model Setup and Validation

3.1 Model Setup

A multilayered and naturally fractured formation with three horizontal BP interfaces (Fig. 6a) and a NF system (Fig. 6b) is established. The model is 600 m long (y-axis), 300 m wide (x-axis), and 120 m thick (z-axis). The three BP interfaces are equally spaced 30 m apart and divide the formation into four layers (layer 1: $z = 0$–30 m; layer 2: $z = 30$–60 m; layer 3: $z = 60$–90 m; and layer 4: $z = 90$–120 m). The NF system that contains 1800 NFs is generated stochastically (Dershowitz and Einstein 1988; Bour et al. 2002; Gale et al. 2007). It exhibits a 0.15-m/m^2 linear density, which is equal to the total length of all NFs divided by the formation area; a random strike angle (θ), corresponding to the intersection angle between the NF and the y-axis; and a 90° dip angle (Fig. 6b). The center point coordinates, lengths, and strike directions of the NFs are drawn from a uniform distribution, a power-law distribution, and a truncated normal distribution, respectively. All NFs are represented by smooth planar rectangles, and the roughness of the real fracture surface is not considered. The length of the NFs ranges from 5 to 20 m, whereas the height of the NFs is fixed at 30 m. The initial aperture of the NFs is related to the average permeability of the NFs (refer to Eq. 19), as shown in Table 1.

Figure 6c shows the model mesh with the triangular prism element, which has an average edge length of 1 m. In the model meshing process, the BP and NF planes are treated as predetermined edges (Grasselli et al. 2015). The final HF pattern is strongly related to the element size and geometry because the HF growth path is limited to the interface between two neighboring elements. Thus, mesh refinement should be performed in the potential regions

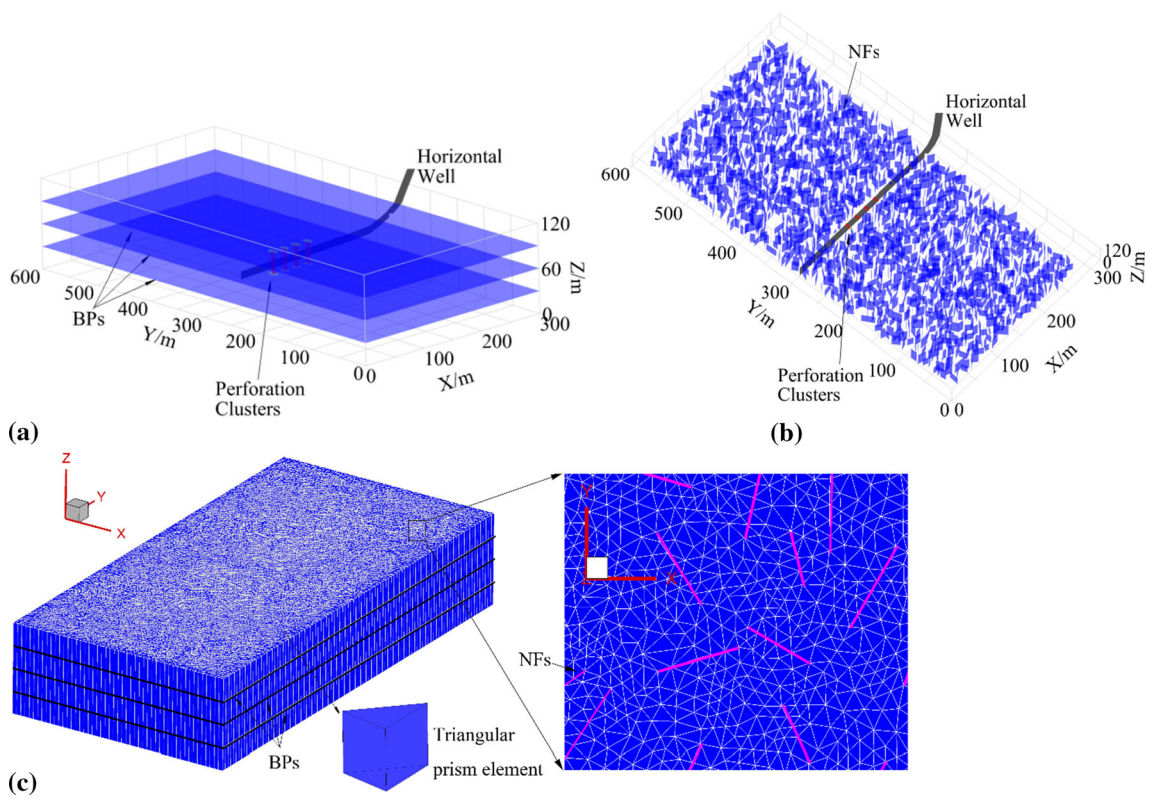

Fig. 6 Layered and naturally fractured shale formation containing **a** three horizontal BP interfaces and **b** a preexisting NF system. **c** Model mesh using triangular prism elements with edges preferentially aligned along the planes of the BPs (*black lines*) and NFs (*pink lines*) (Color figure online)

Table 1 Shale properties used in the numerical simulations

Parameters (symbol)	Unit	Value
Matrix		
Matrix density, ρ	kg/m^3	2600
Permeability, k_h and k_v	μD	1.0; 0.1
Young's modulus, E_h and E_v	GPa	40; 32
Poisson's ratio, ν_h and ν_v	decimal	0.25; 0.2
Tensile strength, T_{0h} and T_{0v}	MPa	8; 5
Cohesion, S_{0h} and S_{0v}	MPa	10; 16
Frictional angle, φ_h and φ_v	°	30; 45
Natural fracture		
Permeability, k_{nf}	μD	50
Tensile strength, T_{0nf}	MPa	1.24
Cohesion, S_{0nf}	MPa	3.75
Frictional angle, φ_{nf}	°	25

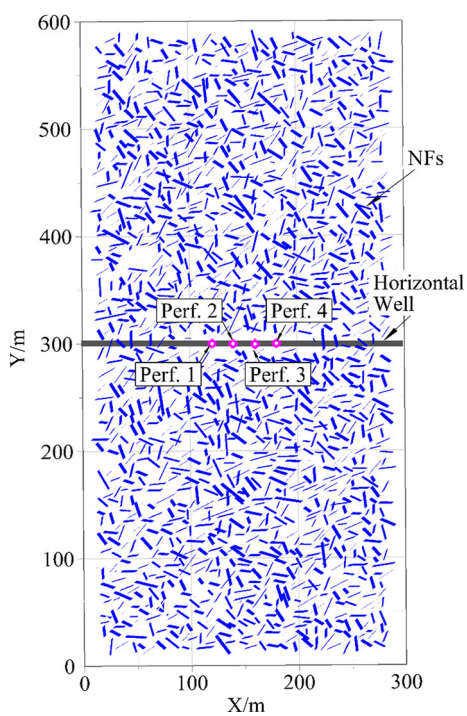

Fig. 7 *Top view* of a horizontal wellbore set along the *x*-axis ($y = 300$ and $z = 55$) and four perforation clusters (Perf. 1, Perf. 2, Perf. 3, and Perf. 4) located at coordinates (120, 300, 55), (140, 300, 55), (160, 300, 55), and (180, 300, 55)

where the fractures may be generated. The reasonable element size can be assessed by comparing the numerical modeling results with the analytical solutions and laboratory test results, which will be presented in Sect. 3.2. The minimum ($\sigma_{h\,min}$) and maximum ($\sigma_{h\,max}$) horizontal stresses as well as the vertical stress (σ_v) were set in the directions parallel to the *x*-, *y*-, and *z*-axes, respectively. A horizontal wellbore was set along the *x*-axis ($y = 300$ and $z = 55$), and four perforation clusters were located at coordinates (120, 300, 55), (140, 300, 55), (160, 300, 55), and (180, 300, 55) (unit: m), as shown in Fig. 7.

3.2 Comparison with Analytical Solutions and Laboratory Tests

The present numerical model is compared with three limiting cases for validation, including a bi-wing HF (with a 120-m fracture height) (Fig. 8a), a horizontal HF (Fig. 8b), and a bi-wing HF intersected by two NFs (with a fracture height of 30 m) (Fig. 9). The constant parameters for all model validations are chosen as follows: $\mu = 5$ MPa s, $Q_t = 5$ m^3/min, $p_{int} = 35$ MPa, $\sigma_v = 50$ MPa, $\sigma_{hmin} = 45$ MPa, and $\sigma_{hmax} = 60$ MPa; however, the third case had $\sigma_{hmax} = 45$–60 MPa.

The growth of a simple bi-wing HF from a horizontal well in an isotropic formation without preexisting discontinuities is initially simulated (Fig. 8a). The average values of the shale properties in the two directions parallel and perpendicular to the BP are chosen for this simulation, e.g., Young's modulus $E = (E_h + E_v)/2$ (Table 1). The data in Table 1 are obtained from laboratory tests of the Longmaxi shale formation (Fig. 1). The comparison of the numerical result with the full length of the HF presented by using the Perkins–Kern–Nordgren (PKN) model without leak-off (Perkins and Kern 1961; Nordren 1972) is shown in Fig. 10a, which displays a 9.8 % error. However, when the formation is considered as a layered and transversely isotropic medium, the HF is completely deflected by a BP interface, resulting in a horizontal fracture (Fig. 8b). The diameter of this horizontal fracture was compared with that calculated by the radial model without leak-off (Perkins and Kern 1961; Geertsma and De Klerk 1969), as shown in Fig. 10a, which exhibits an 11.7 % error. Both the PKN and radial models assumed that the energy required to propagate the fracture was significantly less than that required to allow fluid flow along the fracture, so the rock toughness or rock strength in the fracture growth direction was not considered. In addition, the fluid leak-off was neglected for both the PKN and radial models in the present study, resulting in a high growth rate of the fracture length. Considering a fluid was injected into an unbounded fracture ($T_0 = 0$ MPa) and not allowed to flow into the surrounding joints, our numerical modeling results (fracture length in Fig. 10a and net pressure in Fig. 10b) match well the analytical solutions of the PKN and the radial models. In this case, the error is reduced to 3.6 and 4.9 % for the bi-wing and horizontal HFs, respectively.

The accuracy of this numerical model in simulating the interaction behavior between HF and NF is demonstrated by examining the HF growth path in an isotropic formation (a single layer of 30-m thickness) that contains two NFs

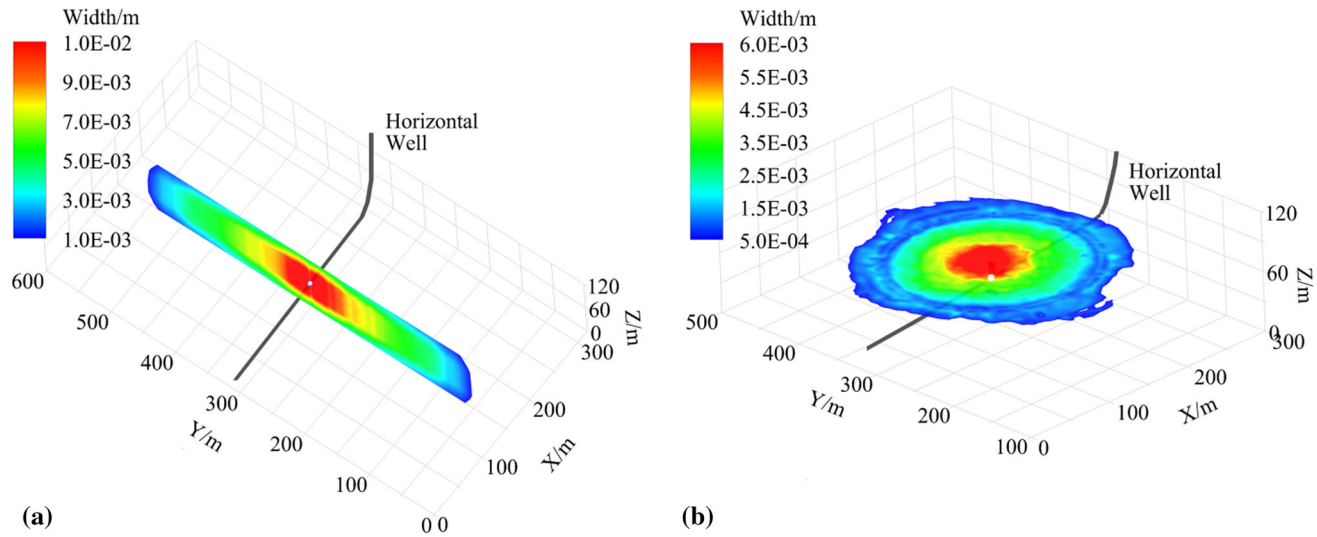

Fig. 8 Fracture geometry under different formation conditions: **a** a simple bi-wing HF growth without considering NFs and BPs; **b** a single horizontal HF growth along the BP interface

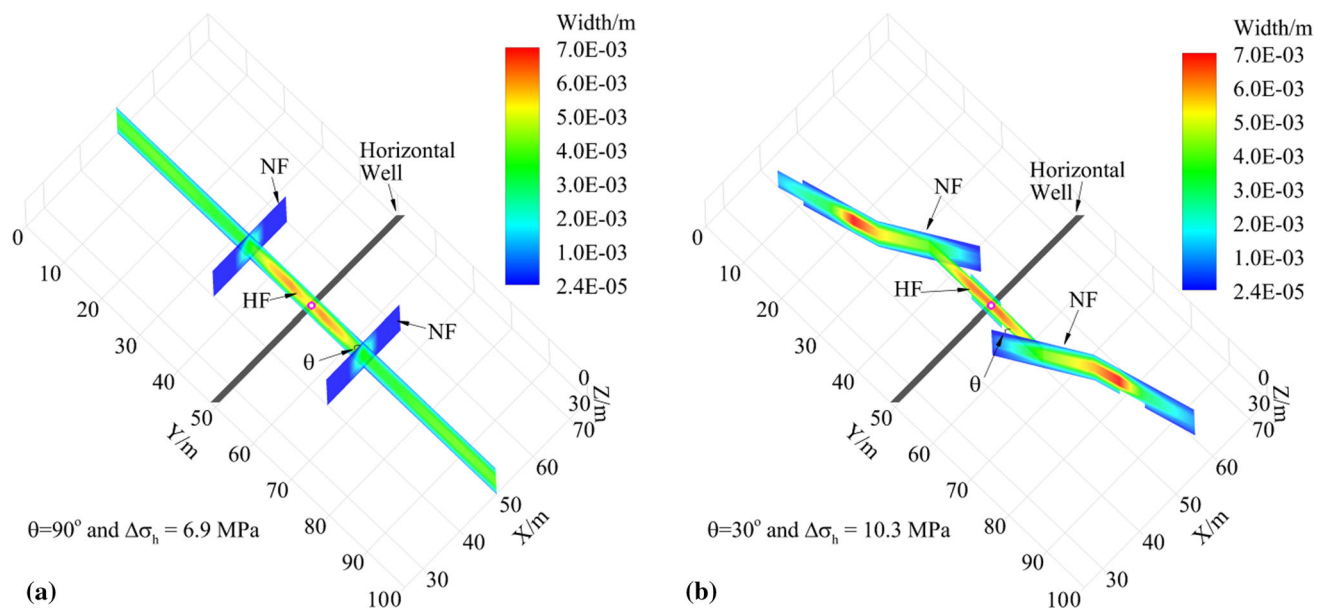

Fig. 9 Two representative results of the HF–NF interaction, **a** HF crossing the NFs without changing the growth path, **b** HF opening the NFs and growing along them

exhibiting the properties mentioned in Table 1. The results are then compared with published experimental data (Blanton 1986; Warpinski and Teufel 1987; Gu et al. 2011). The numerical simulation parameter values are chosen as similar as possible to those used in the experiments in order to establish compatibility between the numerical and experimental results, such as the horizontal stress anisotropy $\Delta\sigma_{\mathrm{h}} = 0 - 15$ MPa ($\Delta\sigma_{\mathrm{h}} = \sigma_{\mathrm{h\,max}} - \sigma_{\mathrm{h\,min}}$) and the intersection angle $\theta = 0^{\circ} - 90^{\circ}$. A series of numerical simulations of the HF–NF interaction are conducted. Figure 9a, b shows two representative results, i.e., the HF crossing the NFs without changing the growth path, and the HF opening the NFs and growing along them (which is similar to the results of HF–BP interaction shown in Fig. 2a, b), respectively. Figure 10c shows all numerical results for the HF–NF interactions at different θ and $\Delta\sigma_h$, which are consistent with the experimental results of Blanton (1986), Warpinski and Teufel (1987) and Gu et al. (2011). Moreover, Fig. 10c demonstrates that the HF tends to cross the NFs under the relatively high $\Delta\sigma_{\mathrm{h}}$ and θ

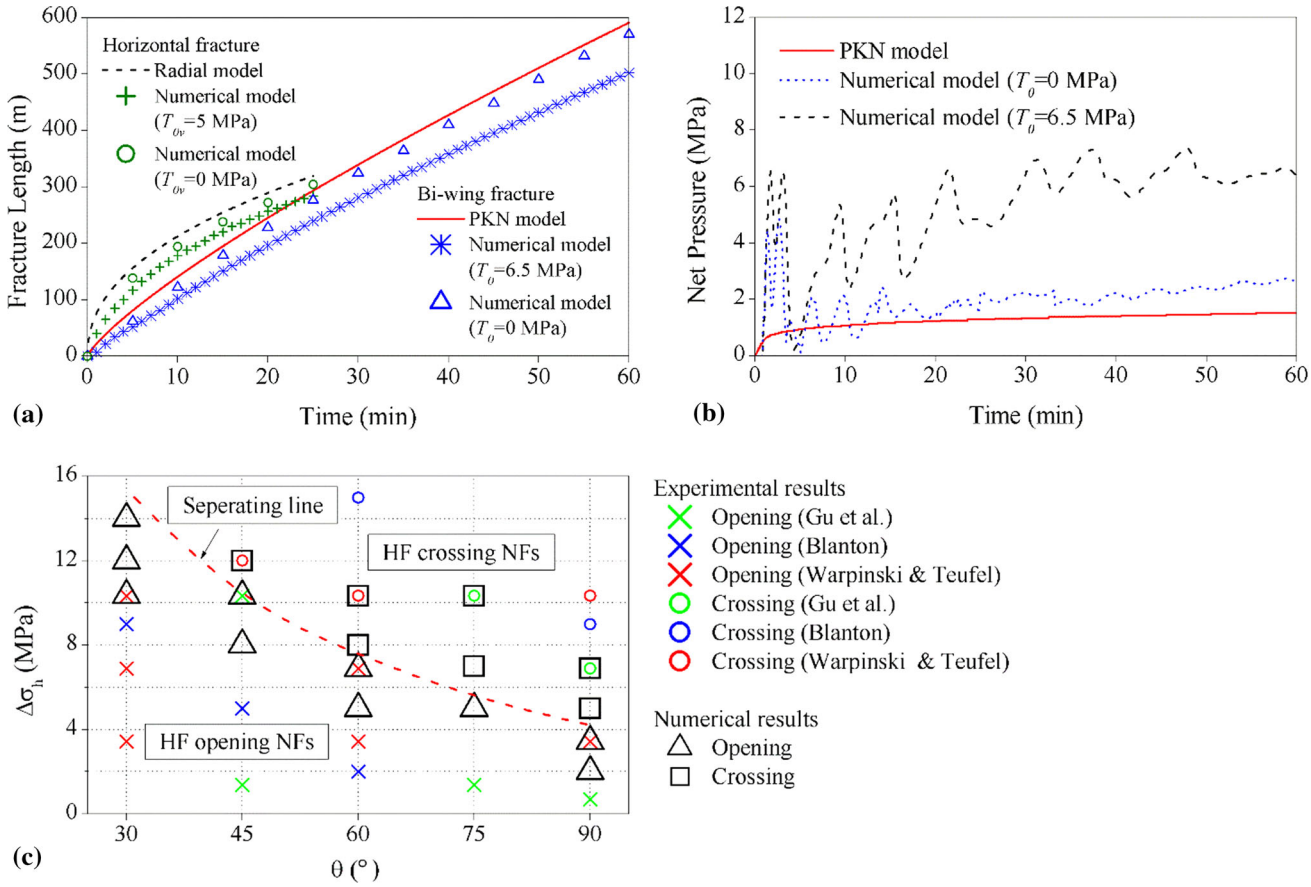

Fig. 10 Comparisons between the numerical model and the PKN model for a bi-wing HF, radial model for a horizontal HF, and experiments for the HF–NF interaction: **a** fracture length versus time curves; **b** net pressure versus time curves; **c** the HF crossing (refer to Fig. 9a) or opening (refer to Fig. 9b) the NFs at different θ and $\Delta\sigma_h$

conditions (on the top right side of the separating line); otherwise, the HF tends to open the NFs under the relatively low $\Delta\sigma_h$ and θ conditions (on the bottom left side of the separating line).

4 Results and Analysis

Based on the configuration shown in Fig. 6, we primarily investigated the effects of vertical stress anisotropy $\Delta\sigma_v(=\sigma_v-\sigma_{h\,min})$, elastic anisotropy E_h/E_v, and strength anisotropy T_{0h}/T_{0v} (set it equal to S_{0v}/S_{0h}) on the HF growth geometry in a layered and naturally fractured shale formation, which was considered an anisotropic medium. The basic shale properties used in numerical simulations are listed in Table 1, and $\sigma_{hmin}=45$ MPa was fixed. We determined the influence of each parameter when its value varied within a range (e.g., $\sigma_{hmax}=45$–65 MPa, $\sigma_v=45$–65 MPa, $E_h=20$–40 GPa, $T_{0v}=0.8$–8 MPa, or $S_{0h}=1.6$ –16 MPa), while all other parameters remained constant. A slick-water fluid of viscosity $\mu=5$ MPa s was pumped for $T=120$ min through four perforation clusters at a rate of $Q_t=12$ m^3/min.

4.1 HF Geometry in an Isotropic Formation Containing a NF System

Figure 11 shows the HF geometries for different horizontal stress anisotropies $\Delta\sigma_h$ in an isotropic formation containing a NF system. When $\Delta\sigma_h$ increases, the resulting HFN is less complex. In the isotropic case of $\Delta\sigma_h=0$ MPa, the HFs that initiated from the four perforation clusters mainly grew along the preexisting NF system, resulting in a highly complex HFN (249 m long in the y-axis direction and 290 m wide in the x-axis direction) near the horizontal wellbore (Fig. 11a). For $\Delta\sigma_h=5$ MPa, the resulting HFN (375 m long and 158 m wide) became longer, narrower, and less complex (Fig. 11b). When $\Delta\sigma_h\geq 10$ MPa, multiple HFs grew mainly along the direction of $\sigma_{h\,max}$, and their growth paths were slightly influenced by the preexisting NF system (Fig. 11c, d). Note that all HFs in the HFN were vertical and had the same height as the formation thickness of 120 m. Moreover, the simultaneously growing HFs from different perforation clusters were relatively isolated in space near the horizontal wellbore. However, these HFs have altered their initial growth paths in the region far from

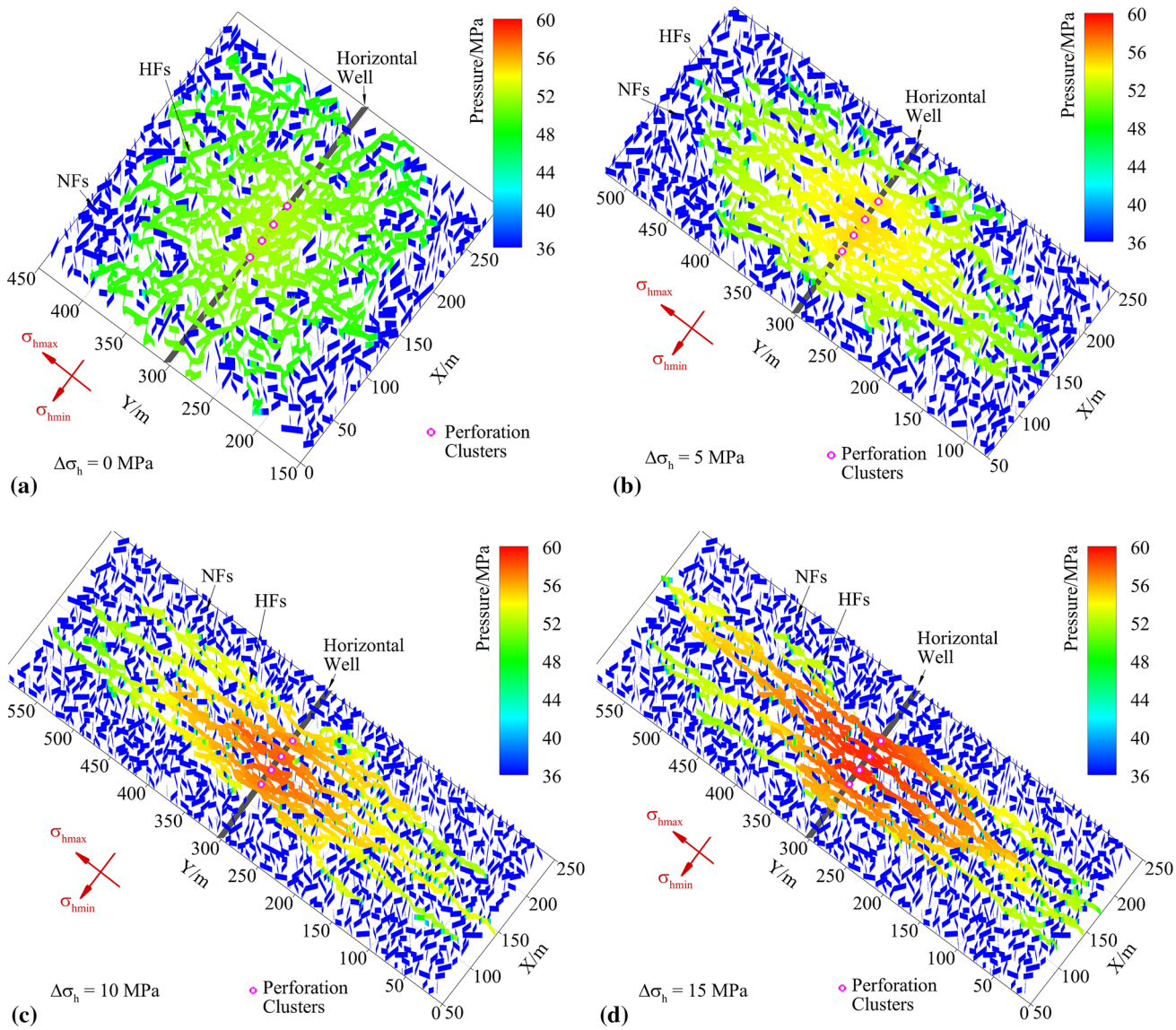

Fig. 11 HF geometry for various horizontal stress anisotropies in an isotropic formation containing a NF system, **a** $\Delta\sigma_h = 0$ MPa, **b** $\Delta\sigma_h = 5$ MPa, **c** $\Delta\sigma_h = 10$ MPa, and **d** $\Delta\sigma_h = 15$ MPa

the horizontal wellbore because of the mechanical interaction among fractures (namely stress shadow), which affects the resulting HF geometry. In fact, the HFs from the exterior perforation clusters located at coordinates (120, 300, 55) and (180, 300, 55) tend to be deflected away from those from the interior perforation clusters located at coordinates (140, 300, 55) and (160, 300, 55) (Fig. 11c, d). Meanwhile, the HFs from the interior perforation clusters tend to merge. Olson (2008) observed that the mechanical interaction among multiple transverse HFs from a horizontal wellbore was closely related to the ratio of net pressure to horizontal stress anisotropy and fracture spacing.

4.2 Influence of Anisotropy on the HF Geometry

The results presented in Sect. 4.1 reveal the difficulty in creating a complex HFN in an isotropic formation containing a NF system when $\Delta\sigma_h > 10$ MPa. Here, we examine how a HF can grow in a layered and naturally fractured formation containing not only a NF system but also the BP interfaces when $\Delta\sigma_h$ reaches up to 15 MPa. A series of numerical simulations with different anisotropies ($\Delta\sigma_v$, E_h/E_v, or T_{0h}/T_{0v}) were performed. Figures 12, 13, and 14 present three representative cases to demonstrate a change from a single horizontal HF to a complex HFN as $\Delta\sigma_v$ increases from 5 to 10 MPa and then to multiple

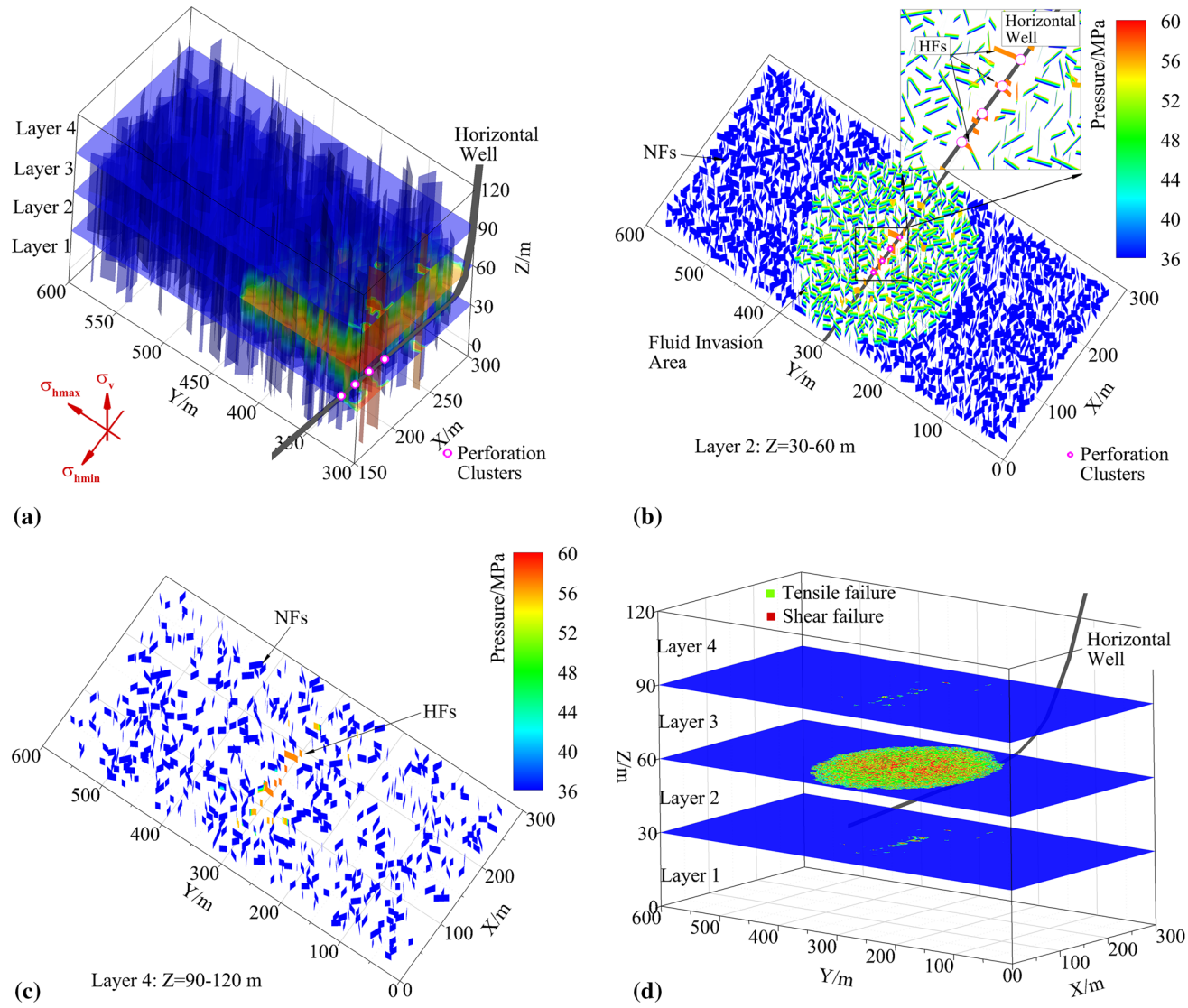

Fig. 12 A single horizontal HF created when $\Delta\sigma_v = 5$ MPa, $E_h/E_v = 1.25$, $T_{0h}/T_{0v} = 10$, and $t = 20$ min: **a** view of HF geometry ($x = 150$ m and $y = 300$ m); **b** HFs initiated *vertically* but cannot propagate far from the perforation clusters of the horizontal wellbore in layer 2 ($z = 30$–60 m); **c** no long fractures are created in layer 4 ($z = 90$–120 m); **d** the weak-strength BP interface ($z = 60$ m) near the *horizontal* wellbore is completely opened in both tensile and shear failure modes

vertical HFs when $\Delta\sigma_v = 15$ MPa. Moreover, Fig. 15 shows the critical conditions determined by all the numerical results for predicting the HF geometry created under a specific anisotropy condition.

Figure 12 demonstrates that a single horizontal HF is created when $\Delta\sigma_v = 5$ MPa, $E_h/E_v = 1.25$, $T_{0h}/T_{0v} = 10$, and $t = 20$ min. Figure 12a–d shows the views of this HF geometry. Multiple HFs can be seen to initiate vertically from the four perforation clusters of the horizontal wellbore in layer 2 (Fig. 12b), but they then stop propagating in both length (or y-axis) and height (or z-axis) and thus cannot grow into the deeper layers (Fig. 12c). This phenomenon is mainly caused because the HFs are deflected into a continuous BP interface ($z = 60$ m) on top of the horizontal wellbore (Fig. 12d). The weak–strength BP interface opens in both tensile and shear failure modes. Meanwhile, a large amount of fracturing fluid from this opened BP interface leaks off into the closed NF system, creating a fluid invasion area, but the NF system cannot be opened in layer 2 (Fig. 12b). Figure 13 shows that a complex HFN is created under the same conditions as in the previous case, but with $\Delta\sigma_v = 10$ MPa and $t = 120$ min. As depicted in Fig. 13b, multiple HFs that initiate vertically from the four perforation clusters of the horizontal wellbore in layer 2 can open and connect with the NF system. Meanwhile, the growing HFs can penetrate through the BP interfaces into adjacent layers

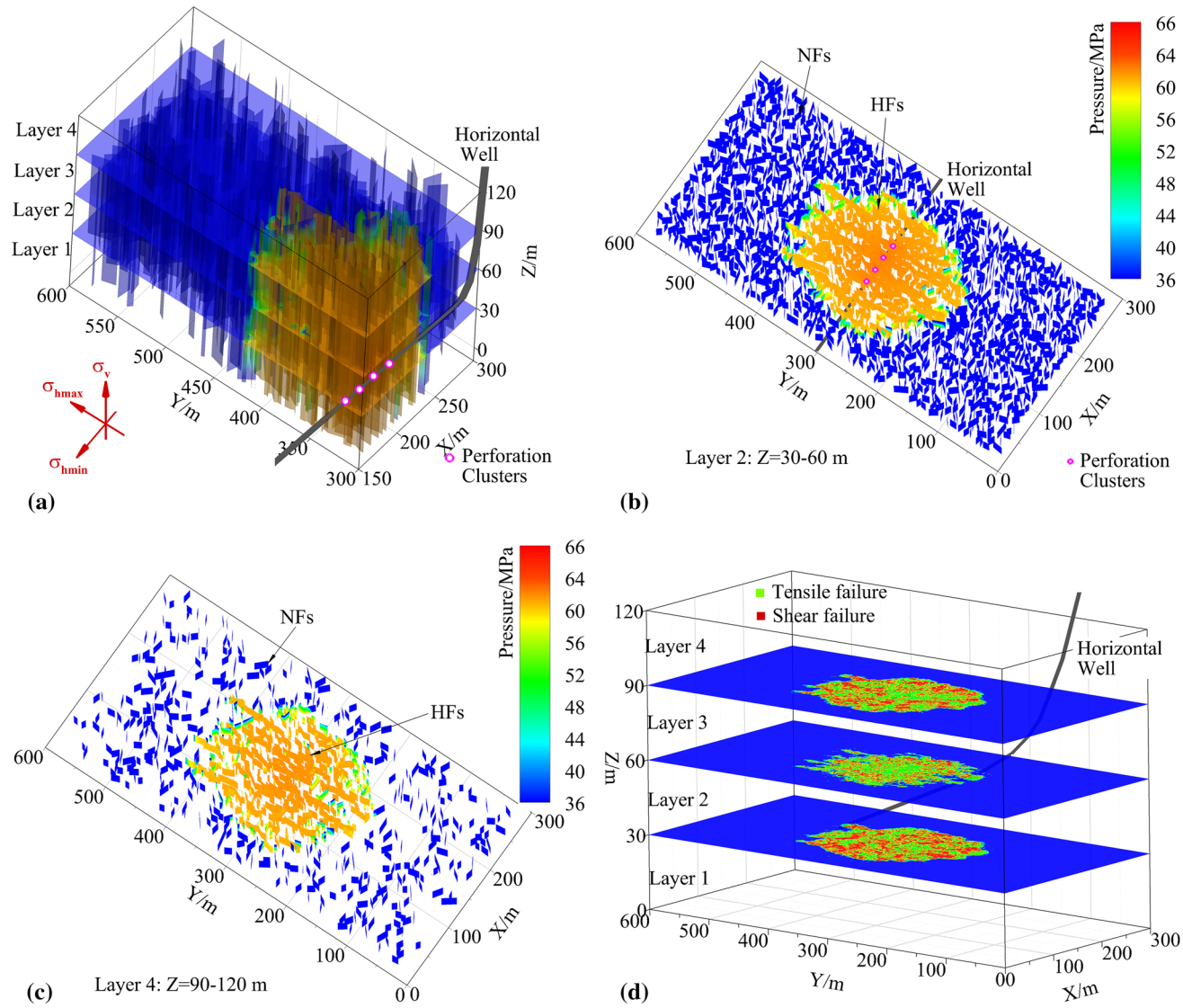

Fig. 13 HFN created in the case of $\Delta\sigma_v = 10$ MPa, $E_h/E_v = 1.25$, $T_{0h}/T_{0v} = 10$, and $t = 120$ min: **a** view of the HF geometry ($x = 150$ m and $y = 300$ m); **b** HFN propagated in layer 2 ($z = 30$–60 m); **c** the resulting HFN in layer 4 ($z = 90$–120 m) becomes less complex because of the decreased amount of opened NFs as compared to those created in layer 2; **d** all the three weak-strength BP interfaces are opened

(Fig. 13c) and induce the BP interfaces to open as well (Fig. 13d). Hence, a complex HFN is generated in this case. However, as the HFN grows into the top (layer 4: $z = 90$–120 m) and bottom (layer 1: $z = 0$–30 m) layers, it becomes less complex because the height growth of certain NFs in the central layer (layer 2: $z = 30$–60 m) is impeded by the top ($z = 60$ m) and bottom ($z = 30$ m) BP interfaces. The occurrence of number of shear failures at the BP interfaces may be responsible for the blunting of the HF tips in the height direction. Interestingly, Rutledge et al. (2014) presented a microseismic mapping result of the Barnett shale where numerous microseismic events were distributed in the pattern of horizontal nodal planes. The authors interpreted the horizontal nodal planes as slip planes that largely followed continuous BP interfaces. When $\Delta\sigma_v$ is up to 15 MPa (and $t = 120$ min), multiple HFs initiated vertically from the four perforation clusters of the horizontal wellbore in layer 2 (see Fig. 14b) and penetrated through the three BP interfaces into adjacent layers without any diversion (Fig. 14d). Although a large amount of fluid could leak out of the HFs into the BP interfaces (Fig. 14a), the HF height growth was not restricted. All the HFs had well-connected pathways between the different layers (Fig. 14b, c) and the same height as the formation thickness of 120 m. The HF growth paths were slightly influenced by both the BP interfaces and the NF system because of the large vertical

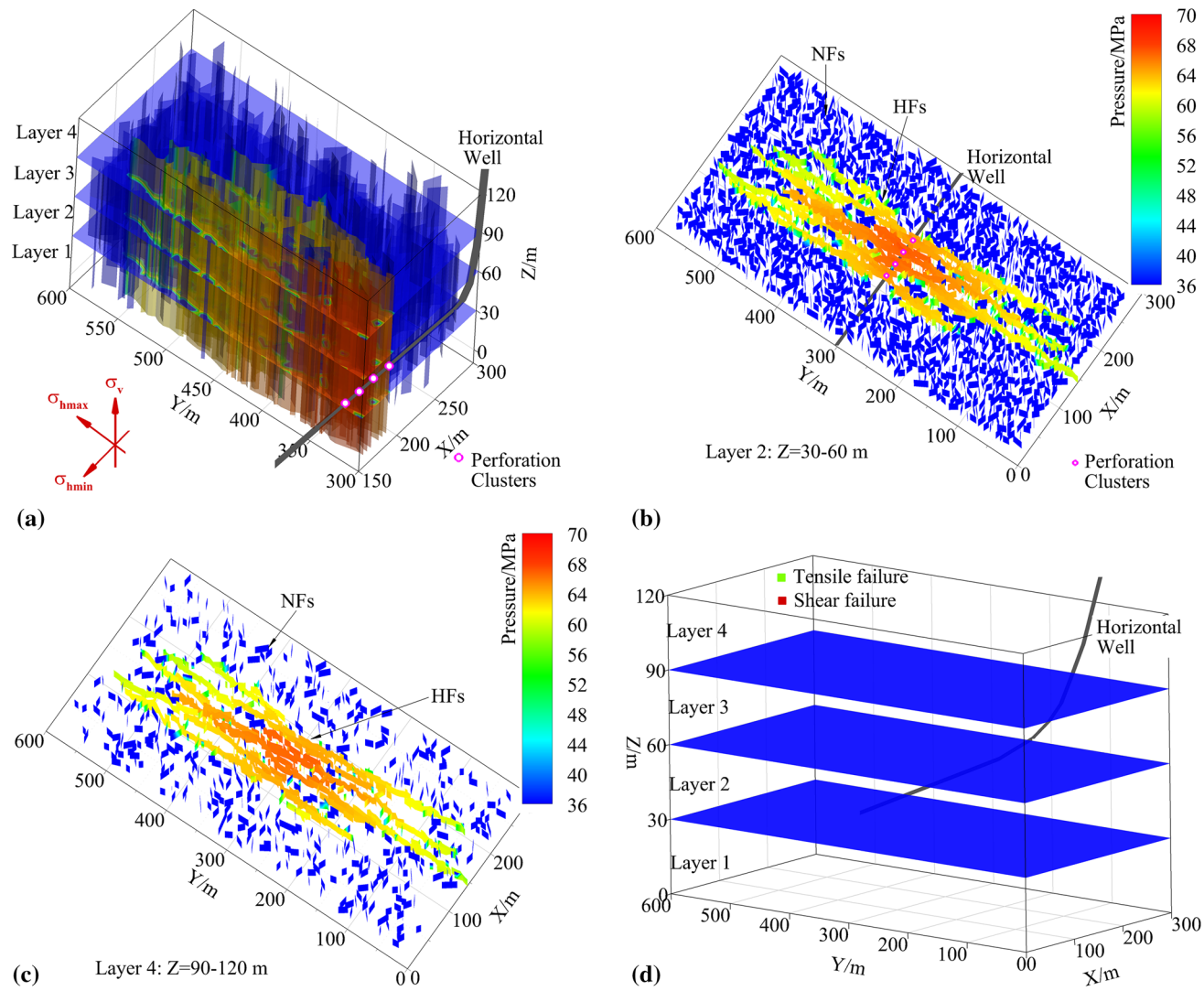

Fig. 14 Multiple vertical HFs created without an obvious diversion into the BP interfaces when $\Delta\sigma_v = 15$ MPa, $E_h/E_v = 1.25$, $T_{0h}/T_{0v} = 10$, and $t = 120$ min: **a** view of the HF geometry ($x = 150$ m and $y = 300$ m); **b** multiple vertical HFs are created in layer 2 ($z = 30$–60 m); **c** the resulting HF geometry in layer 4 ($z = 90$–120 m) is the same as that created in layer 2; **d** no BP interface is opened

($\Delta\sigma_v = 15$ MPa) and horizontal ($\Delta\sigma_h = 15$ MPa) stress anisotropies. As a whole, the HF geometry created in this case was similar to that shown in Fig. 11d.

The results presented here indicate that the BP interfaces significantly influence the HF growth paths, and the HFN can even be created under a high horizontal stress anisotropy ($\Delta\sigma_h = 15$ MPa) in shale formations. It is notable that inducing multiple BP interfaces to open partially is crucial for the HFN creation. The critical conditions related to the anisotropies of elasticity, strength, and vertical stress for the HFs opening or/and crossing the BP interfaces are shown in Fig. 15. Under low $\Delta\sigma_v$ and high T_{0h}/T_{0v} conditions (on the left side of the opening lines), the vertically initiated HFs are likely to be deflected into and grow along a horizontal BP interface, which results in a T-shaped fracture (Fig. 12). In general, the vertical HF area corresponds to a very small part of the entire resulting HF geometry. More specifically, in an elastic isotropic formation ($E_h/E_v = 1$), the creation of a single horizontal fracture occurs under $\Delta\sigma_v \leq 2.5$ MPa for a strength isotropy $T_{0h}/T_{0v} = 1$ and under $\Delta\sigma_v \leq 7$ MPa for a high strength anisotropy $T_{0h}/T_{0v} = 10$. On the contrary, under high $\Delta\sigma_v$ and low T_{0h}/T_{0v} conditions (on the right side of the crossing lines), the HFs can penetrate through the BP interfaces without any division of the fracture path and only a little fluid may leak off into the BP interfaces. In an

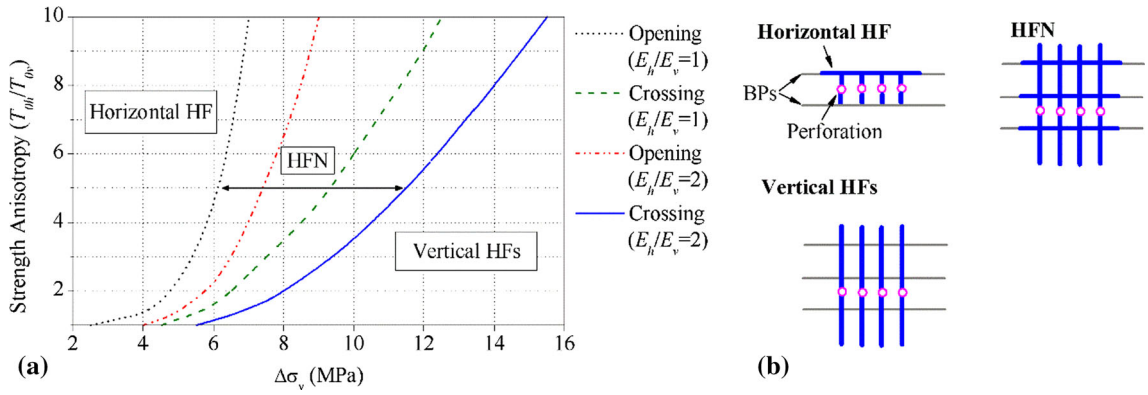

Fig. 15 Prediction of HF geometry for various anisotropies, **a** under low $\Delta\sigma_v$ and high T_{0h}/T_{0v} conditions (on the *left side* of the *opening lines*), HFs can open and deflect into a BP interface; under high $\Delta\sigma_v$ and low T_{0h}/T_{0v} conditions (on the *right side* of the *crossing lines*), HFs can cross a succession of BP interfaces without any diversion; under an intermediate $\Delta\sigma_v$ and T_{0h}/T_{0v}, HFs can cross and open the BP interfaces, resulting in an orthogonal HFN growth; **b** illustration of the three HF geometries: a single horizontal HF, multiple vertical HFs, and a HFN

elastic isotropic formation ($E_h/E_v = 1$), vertical HFs grow without a horizontal component under $\Delta\sigma_v \geq 4.5$ MPa for a strength isotropy $T_{0h}/T_{0v} = 1$ and under $\Delta\sigma_v > 12$ MPa for a high strength anisotropy $T_{0h}/T_{0v} = 10$. Between the above-mentioned two extremes, a potential intermediate state is that the HFs can propagate vertically and branch into the horizontal BP interfaces, which leads to an orthogonal HFN growth. If this orthogonal HFN connected with a NF system, a more complex HFN will eventually be created.

The modeling results mentioned in the preceding paragraphs suggest that the strength anisotropy and vertical stress anisotropy control the HF growth pattern in each layer of the shale formations. Cooke and Underwood (2001) also demonstrated that the strength of the BP interfaces controls the resulting type of HF intersection with BP interfaces. HF deflection is favored at very weak BP interfaces, whereas the HFs propagate straight through the BP interfaces. Meanwhile, the opening of BP interfaces is more likely to occur under a low vertical stress anisotropy; otherwise, the BP interfaces rarely open under a high vertical stress anisotropy, as discussed by Zhang et al. (2007) and Zou et al. (2016). If we also consider the effect of elastic anisotropy for the above-mentioned cases, then the potential for HF branching and fluid invasion into the BP interfaces would obviously increase. Figure 15 shows that for the same strength anisotropy $T_{0h}/T_{0v} = 10$, HFN growth with opened horizontal BP interfaces occurs when $\Delta\sigma_v = 7 - 12$ MPa in an elastic isotropic formation ($E_h/E_v = 1$), whereas it occurs when $\Delta\sigma_v = 9 - 15$ MPa in an elastic anisotropic formation ($E_h/E_v = 2$). Grasselli et al. (2015) also observed that the resulting HFN system is more extensive and complex around a wellbore when the BP interfaces and elastic anisotropy are considered in the model.

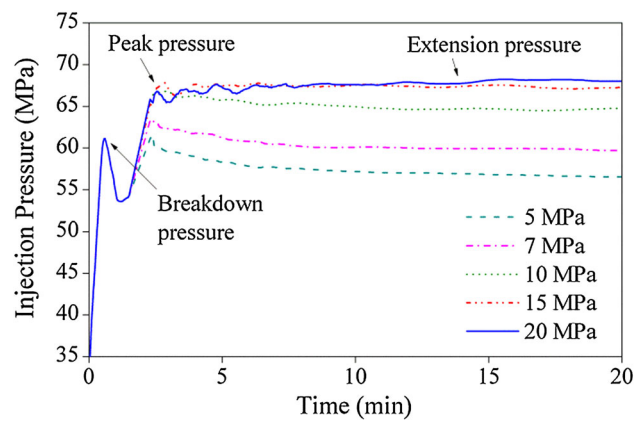

Fig. 16 Injection pressure versus time curves for various vertical differential stresses when $\Delta\sigma_h = 15$ MPa, $E_h/E_v = 1.25$, and $T_{0h}/T_{0v} = 10$

4.3 Influence of Anisotropy on the Injection Pressure

The details of the HF patterns are also reflected in the injection pressure responses. In Fig. 16, the time dependence of the injection pressures is given for various vertical stress anisotropies $\Delta\sigma_v$ when $\Delta\sigma_h = 15$ MPa, $E_h/E_v = 1.25$, and $T_{0h}/T_{0v} = 10$. For all the cases, HFs initiate vertically from the perforation clusters when the injection pressure reaches the breakdown pressure of approximately 62 MPa. When the HFs encounter the horizontal BP interfaces on the top and bottom of the horizontal wellbore, the HF tips and the fluid flow fronts are blunted, limiting the HFs growth in the vertical direction. During this period, the injection pressure rises dramatically until it reaches the peak pressure. After the peak pressure, the injection pressure progressively declines and eventually remains at a relatively low and stable value (extension

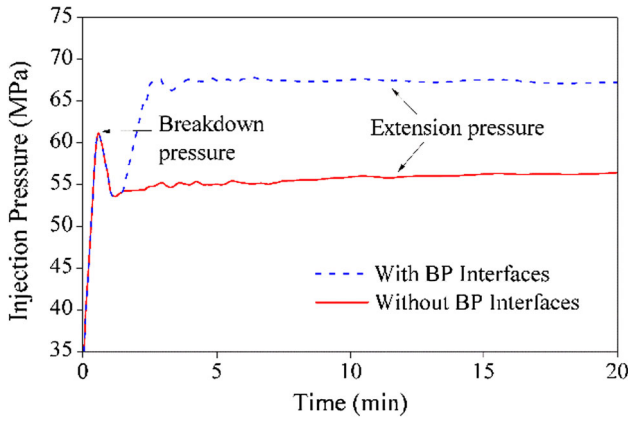

Fig. 17 Injection pressure versus time curves with ($E_h/E_v = 1.25$ and $T_{0h}/T_{0v} = 10$) and without the BP interfaces ($E_h/E_v = 1$ and $T_{0h}/T_{0v} = 1$) when $\Delta\sigma_h = \Delta\sigma_v = 15$ MPa

pressure) when $\Delta\sigma_v < 8$ MPa. This phenomenon can be explained by the fact that the vertically initiated HFs can always be completely deflected into a single BP interface at $z = 60$ m when $\Delta\sigma_v < 8$ MPa, and the fracture growth path and fluid flow path are simple, as shown in Fig. 12. On the contrary, the extension pressure is relatively high and fluctuant when $\Delta\sigma_v > 8$ MPa because the multiple vertical fractures propagate simultaneously and interfere with each other. Note that the magnitude of the peak and extension pressure increases with $\Delta\sigma_v$. This can be explained by the fact that the injection pressure for the growth of a single horizontal HF (when $\Delta\sigma_v < 8$ MPa) or of multiple horizontal HFs existing in the HFN (when $\Delta\sigma_v = 8$–15 MPa) mainly depends on the vertical stress $\Delta\sigma_v$; however, when $\Delta\sigma_v > 15$ MPa, the injection pressure is determined primarily by the minimum horizontal stress σ_{hmin} for the multiple vertical HF growth. Overall, the presence of BP interfaces blunts the HF tips in the vertical direction, so a greater injection pressure is required to induce a large BP-parallel tensile stress on the opposite side of the BP interface from the HF (Fig. 17). Only, if this tensile stress exceeds the BP-parallel tensile strength (the maximum tensile stress criterion is satisfied), can a vertical fracture be re-initiated across the BP interface as expected.

Figure 18 demonstrates that the injection pressure decreases generally and the BP opening width (at $z = 60$ m) increases rapidly as the elastic anisotropy E_h/E_v increases when $\Delta\sigma_v = 7$ MPa, $\Delta\sigma_h = 15$ MPa, and $T_{0h}/T_{0v} = 10$. A high elastic anisotropy value implies that the deformation difference between the directions parallel and perpendicular to the BP is large, and larger deformation is more likely in the direction perpendicular to the BP. Thus, the vertical HFs can be deflected into the horizontal BP interfaces easily, and a large amount of fluid invades into the BP interfaces with large opening width, resulting in a relatively low injection pressure.

5 Conclusions

A numerical approach based on DEM is presented to investigate HFN propagation in a layered and naturally fractured formation such as a shale formation. The inherent BPs and NFs of this formation are captured by inserting a series of horizontally continuous and randomly distributed vertical interfaces, respectively. Various factors are considered in the numerical experiments, including elasticity, strength, and stress anisotropies between the directions parallel and perpendicular to the layer. Three possible cases of HFs intersecting with BPs are presented, including the HF penetration through the BP interface without any diversion, deflection into the BP interface, and simultaneous occurrence of the two previous cases. Therefore, HFN propagation is actually not always vertical, which may result in a dramatically different fracture pattern.

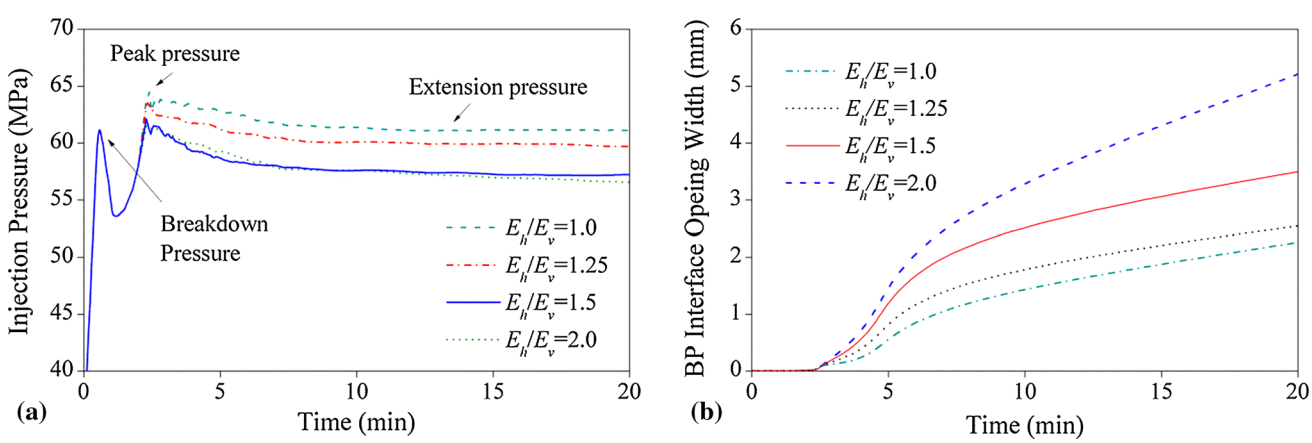

Fig. 18 **a** Injection pressure versus time curves and **b** maximum opening width of the BP interface at $z = 60$ m for various elastic anisotropies when $\Delta\sigma_v = 7$ MPa, $\Delta\sigma_h = 15$ MPa, and $T_{0h}/T_{0v} = 10$

Considering the above-mentioned effects in the model is important for the accurate simulation of the HFN growth pattern in the shale formations.

Low vertical stress anisotropy is favorable in generating a pure horizontal HF along the BP. A relatively low and smooth injection pressure that commonly responds to this horizontal HF creation is insufficient in opening a closed NF system and generating a HFN even under low horizontal stress anisotropy. Vertically growing fractures are more likely to branch into a succession of horizontal BP interfaces for moderate vertical stress anisotropies, and large strength and elastic anisotropies. Although opened BP interfaces restrict the fracture-height growth, they can increase the interconnectivity between the HFs and the NF system, resulting in a complex HFN. At high vertical stress anisotropy, vertical HFs can penetrate through a succession of BP interfaces without any diversion, but the presence of BP interfaces blunts the HF tips and generally increases injection pressure.

Acknowledgments This paper was supported by the Major National Science and Technology Projects of China (No. 2015CB250903) and the National Basic Research Program of China (No. 2013CB228004).

References

Adachi J, Siebrits E, Peirce A, Desroches J (2007) Computer simulation of hydraulic fractures. Int J Rock Mech Min Sci 44(5):739–757

Batchelor GK (1967) An introduction to fluid dynamics. Cambridge University Press, Cambridge

Blanton TL (1986) Propagation of hydraulically and dynamically induced fractures in naturally fractured reservoirs. In: SPE/DOE Unconventional Gas Technology Symposium, Society of Petroleum Engineers

Bour O, Davy P, Darcel C (2002) A statistical scaling model for fracture network geometry, with validation on a multiscale mapping of a joint network. J Geophys Res 107(B6):ETG 4-1–ETG 4-12

Cooke ML, Underwood CA (2001) Fracture termination and step-over at bedding interfaces due to frictional slip and interface opening. J Struct Geol 23(2–3):223–238

Dahi-Taleghani A, Olson JE (2009) Numerical modeling of multi-stranded hydraulic fracture propagation: accounting for the interaction between induced and natural fractures. SPE J 16(3):575–581

Dahi-Taleghani A, Olson JE (2014) How natural fractures could affect hydraulic-fracture geometry. SPE J 19(1):161–171

Dershowitz WS, Einstein HH (1988) Characterizing rock joint geometry with joint system models. Rock Mech Rock Eng 21(1):21–51

Fisher K, Warpinski NR (2012) Hydraulic fracture height growth: real data. In: SPE Annual Technical Conference and Exhibition, Society of Petroleum Engineers

Fisher MK, Davidson BM, Goodwin AK, Fielder EO, Buckler WS, Steinsberger NP (2002) Integrating Fracture mapping technologies to optimize stimulations in the Barnett shale. In: SPE Annual Technical Conference and Exhibition, Society of Petroleum Engineers

Gale JFW, Reed RM, Holder J (2007) Natural fractures in the Barnett shale and their importance for hydraulic fracture treatments. AAPG Bull 91(4):603–622

Geertsma J, de Klerk F (1969) A rapid method of predicting width and extent of hydraulically induced fractures. J Pet Technol 21:1571–1581

Grasselli G, Lisjak A, Omid K, Mahabadi OK, Tatone BSA (2015) Influence of pre-existing discontinuities and bedding planes on hydraulic fracturing initiation. Eur J Environ Civ Eng 19(5):580–597

Gu H, Weng X, Lund JB, Mack GM, Ganguly U, Suarez-Rivera R (2011) Hydraulic fracture crossing natural fracture at non orthogonal angles, a criterion, its validation and applications. In: SPE Hydraulic Fracturing Technology Conference, Society of Petroleum Engineers

Guo TK, Zhang SC, Qu ZQ, Zhou T, Xiao YS, Gao J (2014) Experimental study of hydraulic fracturing for shale by stimulated reservoir. Fuel 128:373–380

Hamidi F, Mortazavi A (2014) A new three dimensional approach to numerically model hydraulic fracturing process. J Pet Sci Eng 124:451–467

Hanson ME, Ronald J, Shaffer RJ, Anderson GD (1981) Effects of various parameters on hydraulic fracturing geometry. SPE J 21(4):435–443

Itasca Consulting Group Inc. (2014) UDEC (universal distinct element code), version 6.0 ICG. Itasca, Minneapolis

Jaeger JC, Cook NGW, Zimmerman RW (2007) Fundamental of rock mechanics, 4th edn. Blackwell Publishing Ltd, Hoboken

Kazerani T, Zhao J (2010) Micromechanical parameters in bonded particle method for modelling of brittle material failure. Int J Numer Anal Methods Geomech 34(18):1877–1895

Lekhnitskii SG (1981) Theory of elasticity of an anisotropic body. Mir Publishers, Moscow

Lisjak A, Grasselli G (2014) A review of discrete modeling techniques for fracturing processes in discontinuous rock masses. J Rock Mech Geotech Eng 6(4):301–314

Meyer BR, Bazan LW (2011) A discrete fracture network model for hydraulically-induced fractures: theory, parametric and case studies. In: SPE Hydraulic Fracturing Conference and Exhibition, Society of Petroleum Engineers

Mokhtari M, Bui BT, Azra N (2014) Tensile failure of shales: impacts of layering and natural fractures. In: SPE Western North American and Rocky Mountain Joint Meeting, Society of Petroleum Engineers

Nagel NB, Sanchez-Nagel MA, Zhang F, Garcia X, Lee B (2013) Coupled numerical evaluations of the geomechanical interactions between a hydraulic fracture stimulation and a natural fracture system in shale formations. Rock Mech Rock Eng 46(3):581–609

Nasehi MJ, Mortazavi A (2013) Effects of in-situs tress regime and intact rock strength parameters on the hydraulic fracturing. J Pet Sci Eng 108:211–221

Nordren RP (1972) Propagation of a vertical hydraulic fracture. SPE J 12(4):306–314

Olson JE (2008) Multi-fracture propagation modeling: applications to hydraulic fracturing in shales and tight gas sands. In: ARMA US Rock Mechanics Symposium

Olson JE, Dahi-Taleghani A (2009) Modeling simultaneous growth of multiple hydraulic fractures and their interaction with natural fractures. In: SPE Hydraulic Fracturing Technology Conference, Society of Petroleum Engineers

Perkins TK, Kern LR (1961) Widths of hydraulic fractures. J Pet Technol 13(9):937–949

Rutledge J, Yu X, Leaney S, Bennett L, Maxwell S (2014) Microseismic shearing generated by fringe cracks and bedding-plane slip. In: SEG Annual Meeting, Society of Exploration

Geophysicists. https://www.onepetro.org/conference-paper/SEG-2014-0896

Suarez-Rivera R, Burghardt J, Stanchits S, Edelman E, Surdi A (2013) Understanding the effect of rock fabric on fracture complexity for improving completion design and well performance. In: SPE International Petroleum Technology Conference, Society of Petroleum Engineers

Thiercelin M, Roegiers JC, Boone TJ, Ingraffea AR (1987) An investigation of the material parameters that govern the behavior of fractures approaching rock interfaces. In: 6th International Congress of Rock Mechanics, International Society for Rock Mechanics

Warpinski NR, Teufel LW (1987) Influence of geologic discontinuities on hydraulic fracture propagation. J Pet Technol 39(2):209–220

Warpinski NR, Kramm RC, Heinze JR, Waltman CK (2005) Comparison of single- and dual-array microseismic mapping techniques in the Barnett shale. In: SPE Annual Technical Conference and Exhibition, Society of Petroleum Engineers

Waters GA, Lewis RE, Bentley DC (2011) The effect of mechanical properties anisotropy in the generation of hydraulic fractures in organic shales. In: SPE Annual Technical Conference and Exhibition, Society of Petroleum Engineers

Weng X (2015) Modeling of complex hydraulic fractures in naturally fractured formation. J Unconv Oil Gas Resour 9:115–134

Weng X, Kresse O, Cohen C (2011) Modeling of hydraulic fracture network propagation in a naturally fractured formation. In: SPE Hydraulic Fracturing Technology Conference and Exhibition, Society of Petroleum Engineers

Xu W, Thiercelin M, Ganguly U (2010) Wiremesh: a novel shale fracture simulator. In: CPS/SPE International Oil and Gas Conference and Exhibition, Society of Petroleum Engineers

Yew CH (1997) Mechanics of hydraulic fracturing. Gulf Professional Publishing, Houston, pp P25–P32

Zhang X, Jeffrey RG (2012) Fluid-driven multiple fracture growth from a permeable bedding plane intersected by an ascending hydraulic fracture. J Geophys Res 117:B12402

Zhang X, Jeffrey RG, Thiercelin M (2007) Deflection and propagation of fluid-driven fractures at frictional bedding interfaces: a numerical investigation. J Struct Geol 29(3):396–410

Zhao Q, Lisjak A, Mahabadi O, Liu Q, Grasselli G (2014) Numerical simulation of hydraulic fracturing and associated microseismicity using finite-discrete element method. J Rock Mech Geotech Eng 6:574–581

Zimmerman RW, Bodvarsson GS (1996) Hydraulic conductivity of rock fractures. Transp Porous Media 23:1–30

Zou YS, Zhang SC, Zhou T, Zhou GT (2016) Experimental investigation into hydraulic fracture network propagation in gas shales using CT scanning technology. Rock Mech Rock Eng 49(1):33–45